# A Biomechanical Approach to Iris Normalization

Inmaculada Tomeo-Reyes[1], Arun Ross[2], Antwan D. Clark[3], Vinod Chandran[1]

[1]Queensland University of Technology, Brisbane, QLD 4000, Australia
{inma.tomeoreyes, v.chandran}@qut.edu.au
[2]Michigan State University, East Lansing, MI 48824, USA
rossarun@msu.edu
[3]West Virginia University, Morgantown, WV 26508, USA
adclark@mail.com

## Abstract

*The richness of the iris texture and its variability across individuals make it a useful biometric trait for personal authentication. One of the key stages in classical iris recognition is the normalization process, where the annular iris region is mapped to a dimensionless pseudo-polar coordinate system. This process results in a rectangular structure that can be used to compensate for differences in scale and variations in pupil size. Most iris recognition methods in the literature adopt linear sampling in the radial and angular directions when performing iris normalization. In this paper, a biomechanical model of the iris is used to define a novel nonlinear normalization scheme that improves iris recognition accuracy under different degrees of pupil dilation. The proposed biomechanical model is used to predict the radial displacement of any point in the iris at a given dilation level, and this information is incorporated in the normalization process. Experimental results on the WVU pupil light reflex database (WVU-PLR) indicate the efficacy of the proposed technique, especially when matching iris images with large differences in pupil size.*

## 1. Introduction

The human iris contains rich texture information defined by distinctive features such as furrows, crypts, ridges, and a zigzag collarette. The textural complexity and variability of the iris across individuals make it a useful biometric trait for recognition of individuals [9].

The goal of an iris recognition system is to compare two irides and generate a match score indicating their degree of similarity or dissimilarity. This process involves five main stages [12]: data acquisition, segmentation, normalization, encoding, and matching. Once a 2D image of the eye has been captured using an iris sensor, the iris region is isolated from other structures in its vicinity during the *segmentation* stage. The resultant iris region is then unwrapped into a rectangular block of fixed dimensions during the *normalization* stage. This stage, which can be regarded as a sampling process, is critical to the success of the subsequent *encoding* and *matching* stages, since it counteracts changes in the size and scale of the iris pattern. The normalized iris image is then subjected to filtering, and the ensuing phasor responses are encoded into a bit string referred to as an iris code. The dissimilarity between two irides is computed using the Hamming distance between their respective iris codes.

The most common normalization method in the literature was proposed by Daugman [4] (see Figure 1). According to Daugman's rubber sheet model, the remapping of the iris image $I(x(r,\theta), y(r,\theta)) \rightarrow I(r,\theta)$ from Cartesian coordinates to a doubly dimensionless pseudo-polar coordinate system can be represented as:

$$x(r,\theta) = (1-r)\, x_p(\theta) + r\, x_s(\theta),$$
$$y(r,\theta) = (1-r)\, y_p(\theta) + r\, y_s(\theta), \quad (1)$$

where $(x_p(\theta), y_p(\theta))$ and $(x_s(\theta), y_s(\theta))$ are respectively the discrete coordinates nearest to the pupillary boundary and the limbic boundary at a given angle $\theta \in [0, 2\pi]$, and $r$ is the normalized radius in the interval $[0, 1]$.
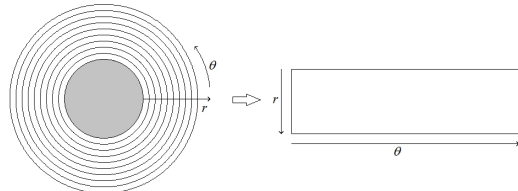


Figure 1: Iris normalization according to the classical rubber sheet model [4].

It is important to note that variations in iris size can be caused due to capturing iris images at different distances or from changes in pupil size. While the rubber sheet model accounts for these variations, it is not robust enough to counteract the degradation of iris recognition performance when certain degrees of pupil dilation occur [11]. This is due to the linear nature of the sampling process being performed during normalization.

As will be explained in detail in Section 2, physiological studies [2, 21] indicate that the deformation of the iris tissue caused by pupil dilation is nonlinear. Therefore, the incorporation of a nonlinear iris normalization scheme will likely address the problems associated with large changes in pupil size. In [22], Yuan and Shi introduced a nonlinear normalization scheme based on the structure of iris fibers proposed by Wyatt [21]. As detailed in the next section, one of the problems of Wyatt's model is that it does not take into account relevant aspects of the iris physiology such as the changes in its elastic properties or the muscle activity. In this sense, Yuan and Shi's approach is limited and other approaches should be explored.

In this paper, a biomechanical model based on the work of Clark *et al*. [2] is used to define a new nonlinear normalization scheme that improves iris recognition performance under various degrees of pupil dilation. Unlike previous models [21], this work takes into account the elastic properties of the iris and the effects of the iris musculature. An example of the efficacy of the proposed normalization scheme can be seen in Figure 2, which illustrates the improvement in genuine match score (Hamming distance or HD) when using the proposed approach versus the classical approach based on the rubber sheet model [4].



(a) Subject #1 before dilation     (b) Subject #1 after dilation

(c) Subject #2 before dilation     (d) Subject #2 after dilation
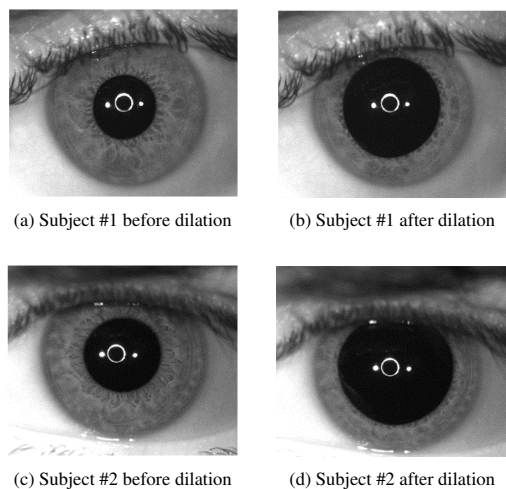
Figure 2: Images from two different subjects before and after pupil dilation. (a) HD (rubber sheet) = 0.424, HD (biomechanical) = 0.3 (29.25% score improvement). (b) HD (rubber sheet) = 0.407, HD (biomechanical) = 0.293 (28.01% score improvement).

## 2. Effect of changes in pupil size: an overview

The effect of changes in pupil size on iris recognition has become an active research topic in recent years, and several factors have been demonstrated to induce varying levels of pupil dilation that negatively affect the performance of iris recognition systems. These factors include changes in the ambient lighting conditions [11], alcohol [1], drugs [5], and aging [6, 8].

According to [11], when the degree of dilation at enrolment is *similar* to the degree of dilation at recognition, the best performance is obtained for highly constricted pupils, whereas the worst performance is obtained for highly dilated pupils. If the degree of dilation is *different* during enrollment and recognition, both dilation and constriction can affect the performance. Recently, Tomeo-Reyes and Chandran [17] performed a bit error analysis on the iris code to investigate the effect of light- and drug-induced pupil dilation and constriction on the consistency of texture information within the iris. Their results showed that bit errors increase by over 10% when comparing a 'normal' image with dilated or constricted images.

Other researchers have focused their attention on mathematically modelling the effects of iris deformation. A number of such approaches are based on the physiology of the iris. In [21], Wyatt presented the 'minimum-wear-and-tear' meshwork, which models iris deformation as a combination of linear and additive nonlinear stretches. The premise of this work is based on [15], in which the iris collagen structure is modelled as a set of fibers arranged in a series of parallel arcs connecting the pupil and iris boundaries in clockwise and counterclockwise directions. As stated by Wyatt, while the proposed model provides a skeleton of the iris, a layer of material needs to be connected to the skeleton to model a real iris.

On the other hand, pattern recognition based approaches have also been used to counteract the effects of iris deformation. From Wyatt's formulation, Wei *et al*. [18] presented a deformation correction method that used a Gaussian function to model the deviation from the linear stretch. In [16], Thornton *et al*. defined a distortion-tolerant similarity metric using the MAP estimate of the parameters of the relative deformation between iris patterns to be matched. Although both approaches improved iris recognition performance, their potential is limited by the fact that they are dependent on the particular dataset used for parameter estimation. Unlike the previous approaches, the nonlinear normalization scheme proposed in this paper is dataset independent.

## 3. Biomechanical model development

From the work of [2], biomechanics [7] can be used to predict the nonlinear dynamics of the iris as a result of pupil

Table 1: Mechanical nomenclature relevant to the definition of the biomechanical model.

| Normal strain $(\epsilon_r, \epsilon_\theta)$ | Normalized deformation acting perpendicular to the material |
|---|---|
| Normal stress $(\sigma_r, \sigma_\theta)$ | Internal forces acting perpendicular to the material |
| Shear stress $(\tau_{r\theta})$ | Internal forces acting tangential to the material |
| Young's moduli $(E_r, E_\theta)$ | Measure of the level of stiffness of an elastic material |
| Poisson's ratio $(\nu)$ | The negative ratio of transverse to axial strain of the material |
| Displacement $(u)$ | The amount of deformation of the material |

dilation. Such an approach complements the classical pattern recognition principles with insights about the muscle activity and the elastic properties of the iris. The relevant notation used for deriving the biomechanical model is summarized in Table 1.

The mathematical formulation of the biomechanical model starts by considering the iris region as a thin cylindrical shell. In this formulation, the $z$ dimension is much smaller than the $r$ and $\theta$ dimensions, so the iris can be viewed as a thin plate where the loads are applied uniformly over the $z$ dimension. It is important to note that, from an iris recognition standpoint, only the two-dimensional perspective in the $r$-$\theta$ plane is considered. Hence, it is assumed that the normal stress in the $z$ direction, $\sigma_z$, and the resulting shear stresses $\tau_{rz}$ and $\tau_{\theta z}$ are negligible. Further, an axisymmetric load is assumed. As a result, the displacement $u$ is independent of $\theta$. Consequently, it follows that the shear stress in the $r$-$\theta$ plane, $\tau_{r\theta}$, is also negligible. It is important to note that soft biological tissues, like the iris, experience finite strain. This formulation approximates this effect by considering nonlinear effects with a linear constitutive law. With these assumptions, the Cauchy-Euler equations [14] that define the strain vector $\vec{\epsilon} = \langle \epsilon_r, \epsilon_\theta \rangle$ reduce to

$$\epsilon_r = u' - \frac{1}{2}(u')^2,$$
$$\epsilon_\theta = \frac{u}{r} - \frac{1}{2}\left(\frac{u}{r}\right)^2, \tag{2}$$

where $u = u(r)$ represents the radial displacement and the primes ()' denote ordinary differentiation with respect to $r$. Also, the equilibrium condition that defines the stress vector $\vec{\sigma} = \langle \sigma_r, \sigma_\theta \rangle$ reduces to

$$\frac{d\sigma_r}{dr} + \frac{\sigma_r - \sigma_\theta}{r} = 0. \tag{3}$$

Adopting Whitcomb *et al.*'s [19] assumption that the iris material is orthotropic, the relationship between the stress and strain vectors, $\vec{\sigma}$ and $\vec{\epsilon}$, is given by (4), where $\nu$ is the Poisson's ratio in the radial direction, $E_r$ and $E_\theta$ are the

Young's moduli in the radial and angular directions, and $\zeta$ is the ratio between them ($\zeta = E_\theta / E_r$).

$$\sigma_r = \frac{E_r}{(1 - \zeta\nu^2)}(\epsilon_r + \zeta\nu\epsilon_\theta),$$
$$\sigma_\theta = \frac{E_\theta}{(1 - \zeta\nu^2)}(\nu\epsilon_r + \epsilon_\theta). \tag{4}$$

Combining equations (2)-(4) yields the following differential equation for the displacement $u(r)$ of the iris tissue within the annular region $r \in (r_1, r_2)$ [2]:

$$u'' + \frac{u'}{r} - \frac{\zeta u}{r^2} - \frac{1 - \nu\zeta}{2r}(u')^2 - \frac{(\nu - 1)\zeta}{2r}\left(\frac{u}{r}\right)^2$$
$$- \frac{1}{2}\frac{d}{dr}(u')^2 - \frac{\nu\zeta}{2}\frac{d}{dr}\left(\frac{u}{r}\right)^2 = 0. \tag{5}$$

Examining (5), it is clear that the iris deformation is nonlinear. Next, an observation is made that, in the $r - \theta$ plane, deformation occurs at the pupillary boundary while the limbus boundary remains stationary. Hence, the boundary conditions in (6) are posed, where $r_1$ and $r_2$ are the resulting pupil and limbus radii respectively.

$$u(r_1) = \mu_1, \mu_1 > 0,$$
$$u(r_2) = 0. \tag{6}$$

Numerical simulation of the radial displacement $u(r)$ calculated from (5) was carried out via the finite element method (FEM). While other numerical methods are also possible, the FEM was chosen due to its flexibility with regard to mesh generation. An example is shown in Figure 3. The FEM implementation consisted of converting (5) into a variational form and discretizing the annular domain into a number of vertices or radial positions where the pupil radius was increased from 2mm to 4.5mm (extreme dilative state). Additionally, the limbus radius was fixed as 6mm. Next, the average material parameters $E_r$ and $E_\theta$ were adopted from Whitcomb *et al.* [19], where $Er = 4$ kPa, and $E_\theta = 2.97$ kPa. From [10], the empirical range for the Poisson's ratio is between 0.45 and 0.5 (i.e., $\nu \in [0.45, 0.5)$). The Poisson's ratio used in this work is $\nu = 0.49$. Comparisons were made by graphing the nonlinear solution $u(r)$ versus the linear solution provided by the rubber sheet model (see Figure 3a). The total deformation was calculated as $r + u(r)$ (see Figure 3b).

## 4. Iris normalization according to the biomechanical model

In this section, a nonlinear normalization method is proposed, which reduces the effect of pupil dilation on iris recognition performance. Unlike the rubber sheet model, in which equally spaced radial samples are considered at each angular position, the proposed method uses the radial
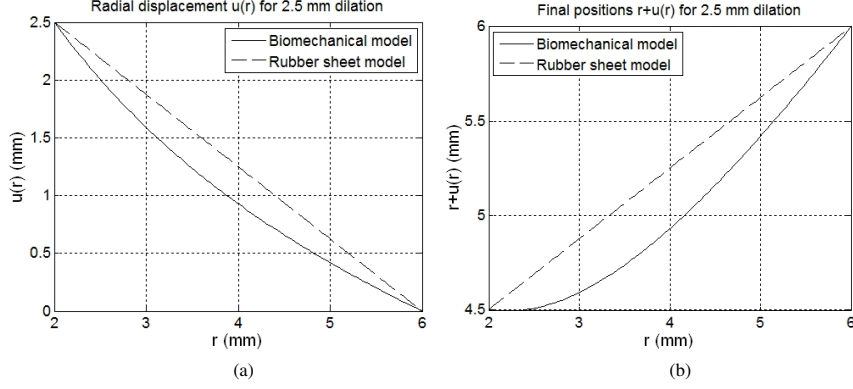
Figure 3: Result of deformation when the pupil radius is increased from 2 mm to 4.5 mm (extreme dilative case) in an iris with a 6 mm-radius limbus. (a) Radial displacement $u(r)$ and (b) final radial positions $r + u(r)$.
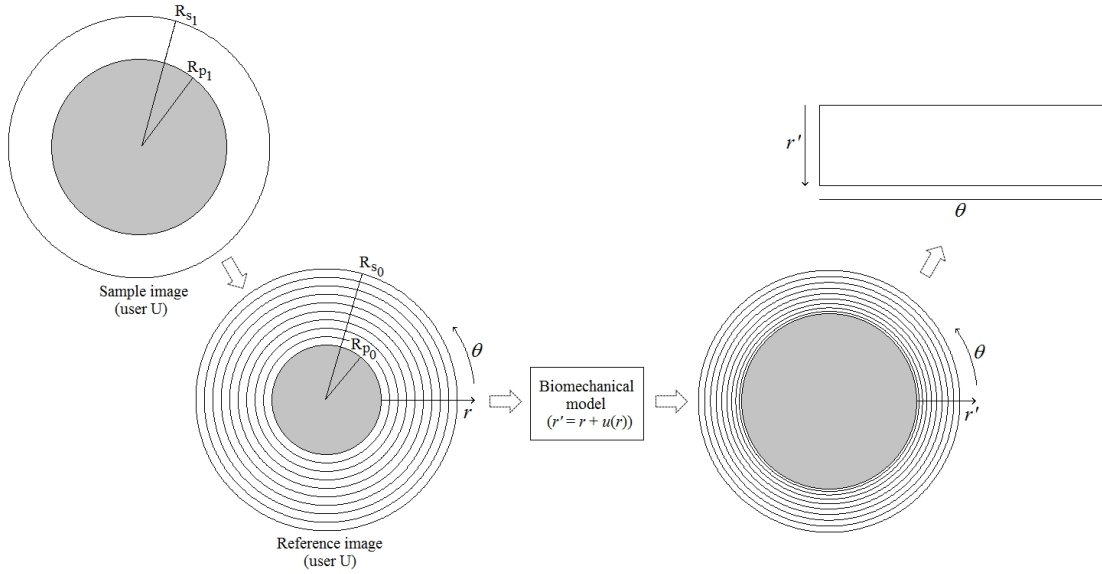


Figure 4: Iris normalization according to the biomechanical model.

displacement estimated by the biomechanical model to perform the radial sampling.

Given an input iris sample with a pupil radius $R_{p1}$, the following process is used to normalize it (see Figure 4):

1. Define the reference image used to estimate the dilation level. In this work, the enrolled image, against which the input iris sample is matched, is used as the reference image. Given the pupil radius of the reference image, $R_{p0}$, the dilation level is calculated as $R_{p1} - R_{p0}$. To avoid any significant impact on recognition speed, the values of the pupil and iris radii of the reference image ($R_{p0}$ and $R_{s0}$, respectively) are pre-computed and stored.

2. Discretize the annular domain defined by $R_{p0}$ and $R_{s0}$ into a number $N$ of uniformly spaced radial positions $r$, where $N$ is the height of the normalized image.

3. At each radial position, $r$, use (5) to solve for $u(r)$.

Use the pupil boundary $R_{p0}$ to start iterating. The ring located at radius $r$ is moved to the final position located at radius $r' = r + u(r)$. The process to numerically simulate $u(r)$ was explained and illustrated with an example at the end of the previous section.

4. Stop iterating once the radius reaches that of the sample image, $R_{p1}$.

5. Use the values of $r'$ to perform the mapping $I(x(r, \theta), y(r, \theta)) \rightarrow I(r, \theta)$ of the iris pixels according to the following equations:

$$r' = r + u(r), \tag{7}$$

$$x(r', \theta) = (1 - r')\, x_p(\theta) + r'\, x_s(\theta),$$
$$y(r', \theta) = (1 - r')\, y_p(\theta) + r'\, y_s(\theta). \tag{8}$$

As in the rubber sheet model (see (1)), the interpolation using the nearest image pixels is bilinear. The addi-
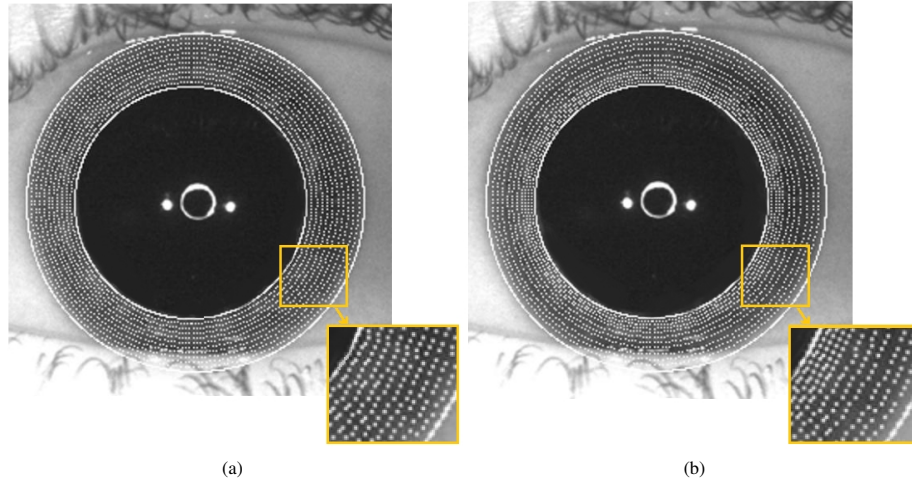
Figure 5: Iris normalization according to (a) rubber sheet model and (b) biomechanical model. White dashed contours represent samples used to create the normalised image.

tional computational demand of the proposed normalization scheme occurs when the radial displacement vector $u(r)$ is computed based on (5). This vector has to be computed for every probe-gallery pair and adds an additional 2.7 ms in computational time compared to the rubber sheet model (time value obtained using MATLAB R2014a-8.3.0.532 and an Intel Core i7 3.4GHz CPU). The difference between the rubber sheet normalization method and the proposed method is illustrated in Figure 5.

## 5. Data and iris recognition algorithm

To evaluate the normalization method, the WVU pupil light reflex database (WVU-PLR) is used [3]. This database includes images from 54 subjects collected under different illumination conditions. A first subset was collected considering a linear increase of light intensity (Experiment A), and a second subset was collected by alternating periods of absence and presence of light (Experiment B). This is the only dataset that we are aware of in which the iris has been subjected to systematic dilation and constriction by application of external light.

Since large differences in pupil size are of interest in the experiments of this research work, only images from Experiment B are considered. In this experiment, images were first captured with a source light off, then on, and then off again, in intervals of approximately 10 seconds. The source light is a tungsten krypton bulb. To guarantee illumination homogeneity, only those images captured while the source light is on are considered. Illumination homogeneity within subjects is important, since it guarantees that none of the results reported in Section 6 are unduly affected by photometric variations on the iris stroma. Finally, only near-infrared (NIR) images are used. The resultant dataset, which will

be referred to as WVU Flash Data Set (WVU-FDS) from here on, consists of 2053 left-eye images from 48 users. Although the initial image resolution is $1392 \times 1040$, images are resized to $640 \times 480$ before processing.

In order to quantify pupil dilation, the ratio between the pupil and iris radii is used. This pupil-to-iris ratio, denoted as $\rho$, will be referred to as dilation ratio throughout this paper (see (9)). While the dilation ratio could in principle vary between 0 and 1, the range of values obtained for the database used is from about 0.2 (highly constricted pupil), to about 0.7 (highly dilated pupil), as depicted in Figure 6. Based on the distribution of $\rho$, images from the WVU-FDS can be divided into three categories: constricted images (blue), images with a normal dilation ratio (yellow), and dilated images (red). Some sample images can be seen in Figure 7. Further details of each category are provided in Table 2.

$$\rho = \frac{pupil\ radius}{iris\ radius}. \tag{9}$$
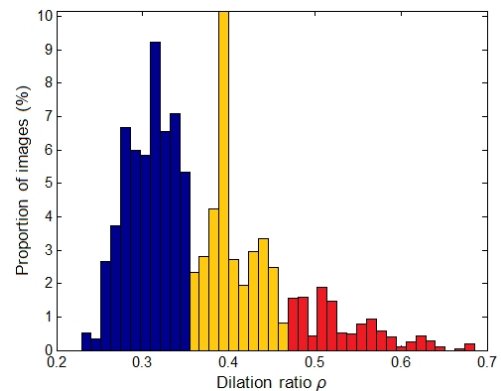


Figure 6: Distribution of dilation ratios in WVU-FDS.
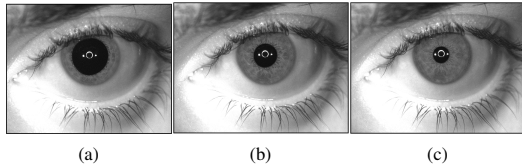
Figure 7: WVU-FDS sample images of the same eye with different dilation ratios. (a) $\rho = 0.62$, (b) $\rho = 0.40$, and (c) $\rho = 0.27$.

Table 2: WVU-FDS categorization according to dilation ratio.

| Conditions | Dilation/constriction level | Dilation ratio | Users | Images |
|---|---|---|---|---|
| Normal | Normal | $0.35 < \rho < 0.475$ | 46 | 776 |
| Dilation | Low | $0.475 \leq \rho < 0.575$ | 40 | 193 |
| | High | $\rho \geq 0.575$ | 17 | 41 |
| Constriction | Low | $0.275 < \rho \leq 0.35$ | 33 | 889 |
| | High | $\rho \leq 0.275$ | 13 | 154 |

According to this categorization, the number of dilated images is considerably lower than that of constricted images. This is due to the image acquisition process. As previously explained, images in the WVU-FDS were collected by alternating periods of absence and presence of light. Images captured right after the source light was activated and a sudden burst of light occurred are dilated, but due to the short pupillary latency they are less numerous. Since the source light is on for 10 seconds, the number of constricted images is considerably higher.

The iris recognition method used in the experiments was proposed by Masek [13] using Daugman [4] and Wildes [20] approaches as a basis. In the segmentation stage, the circular Hough transform is used to locate the pupil and iris boundaries. Eyelids are isolated by fitting a line to them using the linear Hough transform. Eyelashes and reflections are isolated by thresholding. The iris area is normalized to a rectangular grid of dimensions $20 \times 240$. In the feature extraction stage, phase data from 1D Log-Gabor filters is used to represent the texture information. The ensuing phasor responses are quantized, setting two bits of phase information. The resulting iris code has 9600 bits. Iris codes are compared using Hamming distance after barrel-shifting to account for iris rotation.

Two important changes are made with respect to the original algorithm. First, all images from WVU-FDS are automatically segmented and then subjected to a secondary manual segmentation process to refine the mask and minimize any segmentation error. Only minor imperfections, impossible to be eliminated manually, remain. This guarantees that any change in performance is primarily due to the normalization process. The second change involves the replacement of the normalization method in Masek's code with the two methods considered and compared in this paper: the rubber sheet model and the biomechanical model.

## 6. Experimental validation

The performance of the proposed normalization scheme is evaluated on WVU-FDS and compared to that of the rubber sheet model. From the three categories in Table 2, only those images in the 'normal' and 'dilation' categories are analyzed here. The main reason for this is that the current definition of the biomechanical model assumes a positive radial displacement of the pupillary boundary (see (6)) from the resting state, which is defined by a dilation ratio within the normal range. The deformation is then assumed to occur from the resting state. The model is therefore not directly applicable to constriction, unless additional modifications are introduced.

The match scores are calculated using Masek's method in both cases, after manually refining the iris masks to mitigate segmentation errors. Samples from each of the two subsets under analysis (i.e., 'normal' and 'dilated') are compared to a gallery image that exhibits a normal dilation ratio. Consistent with Table 2, the total number of genuine comparisons is 730 in the case of images with normal dilation ratio, and 234 in the case of dilated images. In order to perform cross-validation and obtain a confidence interval, repeated random sub-sampling based validation is used to compute the mean and standard deviation of the matching error rates. Three quarters of the total number of images are randomly chosen to perform the Monte Carlo trials.

### 6.1. Images with normal dilation ratio

For WVU-FDS, dilation ratio values between 0.35 and 0.475 are considered to be within the normal range. The radial displacement in the normalised iris image, which occurs when the pupil dilates from 2.47 mm to 2.88 mm in an iris with a 6 mm-radius limbus, is shown in Figure 8 for both the rubber sheet model and the biomechanical model. This is equivalent to considering dilation ratios between the mean value ($\rho = 0.41$) and the maximum value ($\rho = 0.475$) in the normal range. As observed in the fig-
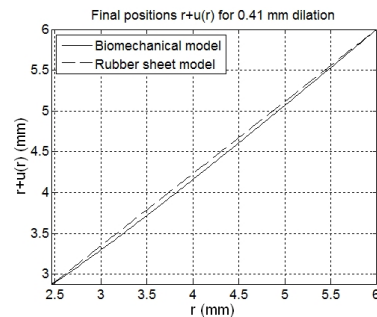


Figure 8: Result of deformation (final radial positions $r + u(r)$) when the pupil dilates from 2.47 mm to 2.88 mm in an iris with a 6 mm-radius limbus. This is equivalent to considering dilation ratios between the mean value ($\rho = 0.41$) and the maximum value ($\rho = 0.475$) in the normal range.
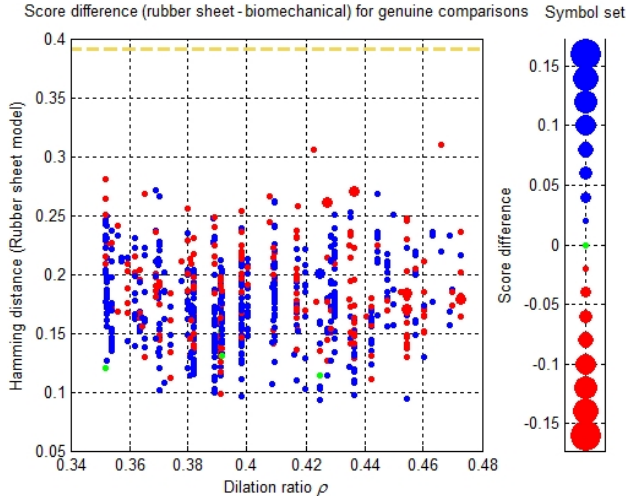
Figure 9: Score difference (rubber sheet model score minus biomechanical model score) for genuine comparisons considering images with **normal dilation ratio**. Red colour represents lower biomechanical model score and blue colour represents lower rubber sheet model score. Low scores are desirable, so the more dots of a certain colour, the better is the corresponding normalization method. The size of the dots represents the difference between the scores, and the dashed yellow line the EER threshold for the rubber sheet model (scores represented in $y$ axis). Since no score is over the threshold, no matching errors occur.

ure, the difference between the two models is quite small, which means that the difference in performance due to the two normalization models is negligible in this normal range.

The small difference in performance between the two models can also be observed in Figure 9. The figure shows the difference between the rubber sheet model scores and the biomechanical model scores for genuine comparisons. Red colour represents lower biomechanical model score and blue colour represents lower rubber sheet model score. Low scores are desirable, since they lead to smaller matching error. This means that the more dots of a certain colour, the better is the corresponding normalization method. The size of the dots represents the magnitude of the difference between the scores. In this case it can be observed that there are more blue dots, which suggests a better performance of the rubber sheet model. However, given the small difference between the scores and the fact that no matching error occurs (all dots are under the EER threshold, represented by a dashed yellow line) it can be stated that both methods lead to identical performance. The False Non Match Rate (FNMR) when the False Match Rate (FMR) equals 0.01 (FNMR@FMR=1%) is zero in both cases.

## 6.2. Dilated images

For the dataset used in these experiments, images with a dilation ratio over 0.475 are considered to be dilated. Unlike the previous case, for this range of dilation ratios, the differ-
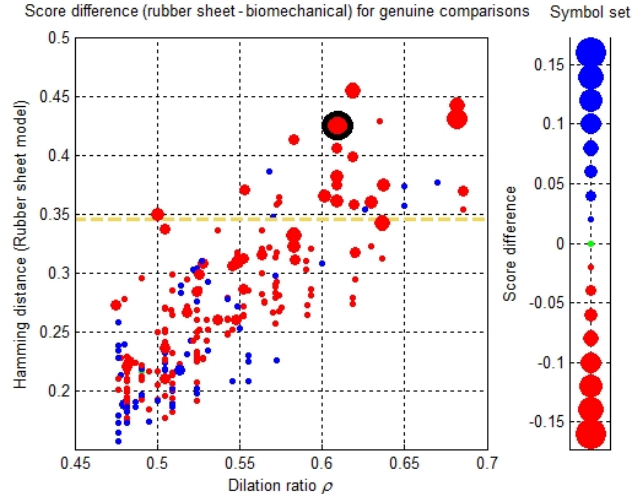


Figure 10: Score difference (rubber sheet model score minus biomechanical model score) for genuine comparisons considering all **dilated images**. In this case, the bigger number and size of the dots associated with the biomechanical model when the dilation ratio is high, shows that the proposed normalization method works better.

ence in deformation calculated by the biomechanical model and the rubber sheet model is quite noticeable. Figure 3, which represents a dilation ratio increase up to $\rho = 0.75$, is a clear example of this. In the case of dilated images, the results obtained when using the biomechanical model clearly outperform those obtained when using the rubber sheet model.

As observed in Figure 10, when the dilation ratio is high, considerably better genuine scores are obtained when using the biomechanical model (most of the dots are red and big). Scores that are in error when using the rubber sheet model (those above the dashed yellow line, which represents the EER threshold of the rubber sheet model), would move below the threshold when using the proposed model provided that the score difference is high enough. This fact turns into lower false reject rates. Consider, e.g., the circled red dot with score equal to 0.42 when using the rubber sheet model. Since the score difference for such a dot equals 0.12, the score obtained with the biomechanical model is 0.35. This score value is under the EER threshold of the rubber sheet model.

Table 3 shows the matching error rate (FNMR@FMR=1%) for the whole dilation dataset, as well as the two subsets of images with low and high dilation ratios. As previously stated, results from the biomechanical model clearly outperform those from the rubber sheet model, with an improvement of the FNMR@FMR=1% from 5.4% to 2% on average when using all the dilated images in WVU-FDS. Results obtained when differentiating between low and high dilation ratios clearly show that the majority of errors are caused by those

images with a high dilation ratio. Since images are matched against gallery images that exhibit normal dilation ratio in the experiments, this is equivalent to stating that most errors occur when matching iris images with highly different dilation ratios. It is in this case where the proposed method is found to considerably improve the matching accuracy, where the FNMR@FMR=1% decreases by 10.5%.

Table 3: Matching error rates (FNMR@FMR=1%) obtained using Masek's method with the whole dilation data set as well as the subsets with low ($0.475 \leq \rho < 0.575$) and high ($\rho \geq 0.575$) dilation ratios.

| Data set | Size (subjects, images) | FNMR@FMR=1% | |
|---|---|---|---|
| | | Rubber sheet | Biomechanical |
| Dilation data set (complete) | (40, 234) | $5.4^{\pm 1.1}$ % | $2^{\pm 0.6}$ % |
| Low dilation ratio | (40, 193) | $1.2^{\pm 0.2}$ % | $0^{\pm 0}$ % |
| High dilation ratio | (17, 41) | $19.4^{\pm 1.4}$ % | $8.9^{\pm 1.7}$ % |

## 7. Conclusions and future work

In this paper, a biomechanical inspired formulation is used to define a new iris normalization scheme. The proposed normalization scheme is compared to the classical rubber sheet model and demonstrated to result in superior accuracy when matching iris images exhibiting significant differences in dilation levels. The FNMR@FMR=1% improves from 5.4% to 2% when using the biomechanical model on WVU-FDS. While linear sampling schemes, such as the one performed by the classical rubber sheet model, are applicable for small variations in pupil size, they are not robust enough to counteract the degradation of iris recognition performance when matching iris images with significantly different dilation ratios. Instead, nonlinear sampling schemes are to be used. This result is reasonable considering the nonlinear nature of iris dynamics.

Future work would include the modification of the biomechanical model to account for pupil constriction, and a thorough analysis of the robustness of the proposed normalization method to inaccuracies in the segmentation process.

## References

[1] S. S. Arora, M. Vatsa, R. Singh, and A. Jain. Iris recognition under alcohol influence: A preliminary study. In *International Conference on Biometrics*, pages 336–341, 2012.

[2] A. D. Clark, S. A. Kulp, I. H. Herron, and A. Ross. A theoretical model for describing iris dynamics. In M. J. Burge and K. W. Bowyer, editors, *Handbook of Iris Recognition*, Advances in Computer Vision and Pattern Recognition, pages 129–150. Springer, 2013.

[3] S. G. Crihalmeanu and A. Ross. Pupil light reflex in the context of iris recognition – Data acquisition setup. Technical report, West Virginia University, 2014.

[4] J. G. Daugman. High confidence visual recognition of persons by a test of statistical independence. *IEEE Transactions on Pattern Analysis and Machine Intelligence*, 15(11):1148–1161, 1993.

[5] L. Dhir, N. E. Habib, D. M. Monro, and S. Rakshit. Effect of cataract surgery and pupil dilation on iris pattern recognition for personal authentication. *Eye*, 224(6):1006–1010, 2010.

[6] M. Fairhurst and M. Erbilek. Analysis of physical ageing effects in iris biometrics. *IET Computer Vision*, 5(6):358–366, 2011.

[7] Y. C. Fung. *Biomechanics: Mechanical properties of living tissues*. Springer, 1993.

[8] P. J. Grother, J. R. Matey, E. Tabassi, G. W. Quinn, and M. Chumakov. IREX VI - Temporal stability of iris recognition accuracy. Technical report, NIST Interagency/Internal Report (NISTIR) 7948, 2013.

[9] P. J. Grother, G. W. Quinn, J. R. Matey, M. L. Ngan, W. J. Salamon, G. P. Fiumara, and C. I. Watson. IREX III - Performance of iris identification algorithms. Technical report, NIST Interagency/Internal Report (NISTIR) 7836, 2012.

[10] J. Heys and V. H. Barocas. Mechanical characterization of the bovine iris. *Journal of Biomechanics*, 32:999–1003, 1999.

[11] K. Hollingsworth, K. W. Bowyer, and P. W. Flynn. Pupil dilation degrades iris biometric performance. *Computer Vision and Image Understanding*, 113(1):150–157, 2009.

[12] A. K. Jain, A. Ross, and K. Nandakumar. *Introduction to biometrics*. Springer, 2011.

[13] L. Masek and P. Kovesi. Matlab source code for a biometric identification system based on iris patterns, 2003.

[14] A. N. Palazotto and S. T. Dennis. *Nonlinear analysis of shell structures*. AIAA Education Services, 1992.

[15] H. Rohen. Der bau der regenbogenhaut beim menschen und einigen sugern. *Gegenbaur Morphology Journal*, 91:140–181, 1951.

[16] J. Thornton, M. Savvides, and V. Kumar. A Bayesian approach to deformed pattern matching of iris images. *IEEE Transactions on Pattern Analysis and Machine Intelligence*, 29:596–606, 2007.

[17] I. Tomeo-Reyes and V. Chandran. Effect of pupil dilation and constriction on the distribution of bit errors within the iris. In *IEEE International Conference on Computer Vision and Pattern Recognition Workshops*, 2014.

[18] Z. Wei, T. Tan, and Z. Sun. Nonlinear iris deformation correction based on gaussian model. In S. W. Lee and S. Z. Li, editors, *Advances in Biometrics*, volume 4642 of *Lecture Notes in Computer Science*, pages 780–789. Springer, 2007.

[19] J. E. Whitcomb, V. A. Barnett, T. W. Olsen, and V. H. Barocas. Ex vivo porcine iris stiffening due to drug stimulation. *Experimental Eye Research*, 89:456–461, 2009.

[20] R. P. Wildes. Iris recognition: An emerging biometric technology. *Proceedings of the IEEE*, 85(9):1348–1363, 1997.

[21] H. J. Wyatt. A 'minimum-wear-and-tear' meshwork for the iris. *Vision Research*, 40:2167–2176, 2000.

[22] X. Yuan and P. Shi. A non-linear normalization model for iris recognition. In *Advances in Biometric Person Authentication*, volume 3781 of *Lecture Notes in Computer Science*. Springer Berlin Heidelberg, 2005.